Multiple-Configuration Quantum/Classical Studies of the Photodissociation Dynamics of H_2O†

Feng Chen and Anne B. McCoy*

Department of Chemistry, The Ohio State University, Columbus, Ohio 43210

Received: February 26, 2003

The photodissociation dynamics of water is investigated, using a quantum/classical treatment. Here, the H + OH dissociation coordinate is treated classically, whereas the dynamics of the remaining OH molecule is propagated quantum-mechanically. It is found that this approach does not provide an accurate description of the dynamics of this system, because of the strong coupling between the quantum and classical coordinates near the transition state. To remedy this situation, a multiple-configuration quantum/classical approach is investigated in which the quantum wave packet is divided into several contributions, each of which is coupled to a separate classical trajectory. This approach is found to provide an accurate representation of the total and partial cross sections for the photodissociation of water on the $\tilde{A}$ state, as well as the OH product state distributions.

I. Introduction

The exact quantum mechanical description of chemical processes can be accurately and relatively easily implemented by solving the time-dependent Schrödinger equation on a well-chosen grid of points.[1,2] Unfortunately, the delocalized nature of quantum mechanical wave functions makes these approaches difficult to implement for systems that contain more than four atoms or six internal degrees of freedom. Moreover, the computational demands of these approaches increase dramatically with the energy that needs to be considered, as well as with the effective masses that are associated with the internal motions. This is because an increase of either of these quantities increases the density of the grid points that is required to obtain accurate results. In contrast, classical treatments scale approximately linearly with the dimensionality of the system. Furthermore, in the limits where quantum approaches become less efficient, at high energies or for heavier atoms, quantum mechanical effects, such as tunneling and zero-point energy, tend to become less important. In many systems, particularly those which include H atoms, some of the dynamical properties are described well by classical approaches, whereas a small subset of the degrees of freedom requires a quantum mechanical treatment.

On the basis of the previously mentioned analysis, an attractive alternative to purely quantum mechanical or classical approaches is to propagate a small subset of the degrees of freedom quantum-mechanically, while the remaining degrees of freedom are treated classically.[3−8] Here, the quantum and classical subsystems evolve time-dependently and they are coupled through the time-dependent self-consistent field (TDSCF) approximation.[3]

To justify this division of the system into quantum and classical parts, a minimal degree of separability between the dynamics of the quantum and classical subsystems must be assumed. A serious drawback of the simplest quantum/classical treatments comes from the fact that, if the dynamics of the two subsystems is not sufficiently separable, the quantum/classical approximation can lead to an artificial correlation in the dynamics of the two subsystems.

Similar problems have been reported for the analogous quantum/quantum TDSCF approximation.[9] To minimize the effects of this overcorrelation in the TDSCF approach, multiple-configuration extensions have been suggested and successfully implemented for a variety of problems.[9−12] Recently, we have proposed a similar approach for quantum/classical studies.[8,13−15] In this approach, the quantum subsystem is divided into two or more orthogonal wave functions and separate classical trajectories are propagated for each of the contributions to the quantum wave packet. This approach can provide an accurate description of the dynamics, whereas the computational demands of the simulation are not significantly greater than those for a single-configuration treatment.

In this paper, we will investigate single- and multiple-configuration approximations to the photodissociation dynamics of H_2O on the $\tilde{A}$ electronic state. We choose this system for several reasons. First, it is a system that has been investigated by a variety of computational approaches, including time-dependent quantum calculations[16−18] and classical trajectory simulations.[19,20] As such, it provides an attractive system on which to benchmark the multiple-configuration quantum/classical approach. In addition, the photodissociation of water has been an area of almost-continuous experimental interest for the past 25 years.[21−27] Recently, studies of the photodissociation of water in clusters have been reported,[28−30] thereby presenting situations in which purely quantum treatments of the dynamics are no longer feasible. Finally, the symmetry of the photodissociation of water, in which either of the two OH bonds can be broken with equal probability, makes this system a particularly challenging one for quantum/classical treatments. In fact, we find that, in the single-configuration treatment, the overcorrelation between the quantum and classical degrees of freedom can cause trajectories to be trapped in the transition state of the purely repulsive $\tilde{A}$-state potential surface. On the other hand, the fact that the photodissociation of water is prompt and there are strong correlations between the OH stretching and bending vibrational motions on the $\tilde{X}$ state and the rotational and

† Part of the special issue "Donald J. Kouri Festschrift".

* Author to whom correspondence should be addressed. E-mail: mccoy@chemistry.ohio-state.edu

10.1021/jp034498d CCC: $25.00
Published on Web 05/10/2003

vibrational distributions of the OH product make this process well-suited for testing the accuracy of quantum-classical treatments of the dynamics.[24,26,31]

The remainder of this paper is organized as follows. In the next section, we develop the quantum/classical treatments that will be used to describe the dynamics. Calculations of the absorption spectrum of photodissociation of H_2O are presented in detail in section III. Here, we will compare the results of various forms of multiple-configuration quantum/classical approximation to those obtained from numerically exact calculations. Conclusions are given in section IV.

II. Theoretical Approaches

A. Coordinates and the Hamiltonian. In this study, the photodissociation dynamics of water is described in terms of the atom−diatom Jacobi coordinates (R,r,θ). Here, R provides the distance between one of the H atoms and the center of mass of the other OH fragment, r provides this OH distance, and θ is the angle between the vectors associated with R and r. The vibrational ($J = 0$) Hamiltonian in these coordinates is given by

$$\hat{H} = -\left(\frac{\hbar^2}{2\mu_R}\right)\frac{\partial^2}{\partial R^2} - \left(\frac{\hbar^2}{2\mu_r}\right)\frac{\partial^2}{\partial r^2} + \left(\frac{1}{2\mu_R R^2} + \frac{1}{2\mu_r r^2}\right)\hat{j}^2 + V(R,r,\theta) \tag{1}$$

where μ_R and μ_r are the reduced masses for H−OH and OH, respectively, and $V(R,r,\theta)$ provides the global potential surface for water. In this study, we use the high-quality ab initio surface of Partridge and Schwenke[32] to describe the $\tilde{X}$ state and the potential of Engel and co-workers[16] is used to describe the $\tilde{A}$ state. Finally, the volume element for integration is given as $\sin\theta\ \mathrm{d}r\ \mathrm{d}R\ \mathrm{d}\theta$.

Because we are considering the photodissociation dynamics of water from a specific vibrational state on the $\tilde{X}$ electronic state, we must first evaluate the wave functions and energies using the $\tilde{X}$-state potential surface. After the wave functions are obtained, we use time-dependent quantum and quantum/classical approaches to propagate the dynamics on the $\tilde{A}$ electronic state. Here, quantum approaches refer to studies in which all three coordinates are treated quantum-mechanically. In the quantum/classical studies, the dynamics in r and θ are treated quantum-mechanically, whereas the dynamics in R and its conjugate momentum P are treated classically. As such, the study proceeds through two steps. In the first part, we evaluate the wave function for the state that corresponds to the initial conditions for the photodissociation dynamics; in the second part, we consider the photodissociation dynamics.

B. Determination of the Initial Conditions. The wave function will be represented on a grid for the quantum dynamics simulations; therefore, it is convenient to use a grid-based approach to evaluate the wave functions on the $\tilde{X}$ state as well. There are several approaches that can be employed. A common choice is to employ a relaxation approach, as was described by Kosloff and co-workers.[33] Although this approach is efficient for the ground and other low-lying vibrational states, it becomes less attractive if a range of vibrational states is intended to be investigated. As such, we choose to evaluate the ground-state wave function in a discrete variable representation (DVR),[34,35] in which the wave function is represented on a three-dimensional grid of points. For the two radial coordinates r and R, we employ an evenly spaced grid of points, as described by Colbert and Miller,[36] whereas a DVR that is based on the Legendre polynomials is used to describe the bending dependence of the wave function.

Because the vibrations of water are well-described by a local mode model,[37] we evaluate the energies and wave functions for the $\tilde{X}$ state of water in two steps.[38,39] In the first step, we evaluate the eigenfunctions and eigenvalues of the three one-dimensional Hamiltonians, obtained by setting the remaining two coordinates to the values that correspond to the minimum in the potential:

$$\begin{aligned}
\hat{h}_R &= -\left(\frac{\hbar^2}{2\mu_R}\right)\frac{\partial^2}{\partial R^2} + V(R,r_e,\theta_e)\\
\hat{h}_r &= -\left(\frac{\hbar^2}{2\mu_r}\right)\frac{\partial^2}{\partial r^2} + V(R_e,r,\theta_e)\\
\hat{h}_\theta &= \left(\frac{1}{2\mu_R R_e^2} + \frac{1}{2\mu_r r_e^2}\right)\hat{j}^2 + V(R_e,r_e,\theta)
\end{aligned} \tag{2}$$

The full Hamiltonian matrix is then set up in a direct-product basis of the eigenfunctions of the Hamiltonian operators in eq 2. By only including a subset of the possible direct product functions, for example, those for which the diagonal matrix elements are smaller than a cutoff energy, one can obtain converged energies by diagonalizing relatively small matrices. Furthermore, because

$$\begin{aligned}
\hat{H} = \hat{h}_R + \hat{h}_r + \hat{h}_\theta + \left(\frac{1}{2\mu_R R^2} - \frac{1}{2\mu_R R_e^2} + \frac{1}{2\mu_r r^2} - \frac{1}{2\mu_r r_e^2}\right)\hat{j}^2 +\\
V(R,r,\theta) - V(R,r_e,\theta_e) - V(R_e,r,\theta_e) - V(R_e,r_e,\theta)
\end{aligned} \tag{3}$$

all the required integrals either involve only one of the three coordinates or, in the case of the full potential, can be evaluated numerically using the value of the wave function at each of the grid points.

Although the previously described approach provides accurate energies and wave functions for the vibrational states of water, the resulting wave functions are not in a convenient form if we wish to employ a separation of the dynamics into the quantum-mechanical OH rotations and vibrations and the classical H atom translations. Here, we need to represent the wave function as a product of two wave functions: one that depends on r and θ, and one that is a function of R. These wave functions are obtained by expanding the eigenfunction of $\hat{H}$ in eq 3 in a natural modal basis.[40] This basis is designed to maximize the leading coefficient in the expansion. The natural modal basis functions are obtained from the eigenfunctions of the Hamiltonian matrix by first setting up the two density matrices:

$$\rho_R^{(n)}(R,R') = \int\int \sin\theta\ \mathrm{d}\theta\ \mathrm{d}r\ \Psi_n^*(R,r,\theta)\Psi_n(R',r,\theta) \tag{4}$$

$$\rho_{r,\theta}^{(n)}(r,\theta,r',\theta') = \int \mathrm{d}R\ \Psi_n^*(R,r,\theta)\Psi_n(R,r',\theta') \tag{5}$$

The eigenfunctions of these matrixes, $\{\psi^{(n)}(R)\}$ and $\{\chi^{(n)}(r,\theta)\}$, provide the natural modal basis functions. In the discussion that follows, we will represent this approximation to $\Psi_n(R,r,\theta)$ by the $\psi(R)\chi(r,\theta)$ product state that has the largest overlap with $\Psi_n(R,r,\theta)$. In the case of the ground state of water, we find that the overlap between $\Psi_n(R,r,\theta)$ and $\psi(R)\chi(r,\theta)$ is >0.9996, whereas for the states with four quanta in the OH stretch, it exceeds 0.9577.

C. Quantum Simulations. To quantify the accuracy of the quantum/classical treatments, we first perform quantum simulations of the dynamics by solving the relation

$$\Phi(R,r,\theta,t) = \exp\left(-\frac{i\hat{H}t}{\hbar}\right)\Phi(R,r,\theta,t=0) \tag{6}$$

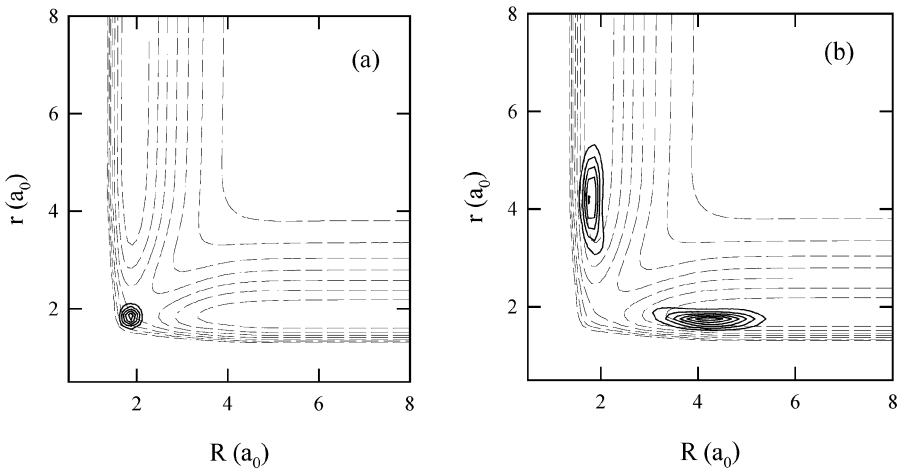

Figure 1. Snapshots of the wave packet for H_2O at t = (a) 0 and (b) 400 au. These plots are superimposed on the $\tilde{A}$-state potential energy surface for water (dashed lines).[16] Here, the contours are spaced by 0.02 hartree with the highest energy contour located at 0.14 hartree.

For the purposes of the present study, we will refer to the results of these simulations as exact, to quantify the accuracy of the quantum/classical approaches. The same grid representation of the wave function is used for these calculations as was used to evaluate the wave functions on the $\tilde{X}$ state. The wave function is then propagated using a Chebychev expansion of the propagator in eq 6.[2,41] Fast Fourier transforms are used to transform the radial parts of the wave function between coordinate- and momentum-space representations,[1] whereas a transformation matrix is used to transform the angular dependence from a DVR to the finite basis representation.[42]

D. Mixed Quantum/Classical Treatments. In the quantum/classical approach, the system is divided into two subsystems: one is treated quantum-mechanically, whereas the other is treated classically. For the photodissociation of water, the coordinate and momentum of one of the H atoms (R and P, respectively) are propagated classically, whereas the dynamics of the remaining OH molecule, which is described by r, θ, and their conjugate momenta, is propagated quantum-mechanically.

Although the motions of one of the H atoms can be treated classically, as Schinke and Heller have shown,[19,43] the initial conditions for these trajectories must reflect the initial quantum state of the system, if we are to obtain a meaningful description of the photodissociation dynamics. Following Heller and Schinke and their co-workers, we map the R dependence of the initial wave function, $\psi(R)$, onto a phase space distribution using the Wigner function:[43,44]

$$W(R,P) = \frac{1}{2\pi\hbar}\int_{-\infty}^{+\infty} \mathrm{d}s\ \psi^*\left(R+\frac{s}{2}\right)\psi\left(R-\frac{s}{2}\right)\exp\left(\frac{isP}{\hbar}\right) \quad (7)$$

where $W(R,P)$ provides the relative weights of each trajectory. In the present work, we select our initial conditions from an evenly spaced grid of points in R and P and run only those trajectories for which the magnitude of the $W(R,P)$ exceeds 10^{-3}. It should be noted that the Wigner function has an uncomfortable feature: it may have negative values. We find that, by including trajectories with both positive and negative weights in our simulation, we obtain partial cross sections that are in good agreement with the results of the full quantum treatment.

After the initial coordinates, momenta, and weights are generated, the quantum/classical trajectories are then propagated by numerically solving the equation[6]

$$i\hbar\frac{\partial\chi(r,\theta,t)}{\partial t} = \left\{-\left(\frac{\hbar^2}{2\mu_r}\right)\frac{\partial^2}{\partial r^2} + \left[\frac{1}{2\mu_r r^2} + \frac{1}{2\mu_R R^2(t)}\right]\hat{J}^2 + V(R(t),r,\theta)\right\}\chi(r,\theta,t)$$

$$\frac{\mathrm{d}R(t)}{\mathrm{d}t} = \frac{P(t)}{\mu_R}$$

$$\frac{\mathrm{d}P(t)}{\mathrm{d}t} = -\frac{\left\langle\chi(r,\theta,t)\left|\frac{\partial\hat{H}}{\partial R}\right|\chi(r,\theta,t)\right\rangle}{\langle\chi(r,\theta,t)|\chi(r,\theta,t)\rangle} = -\frac{\left\langle\chi(r,\theta,t)\left|\frac{\partial V(R(t),r,\theta)}{\partial R} - \frac{\hat{J}^2}{\mu_R R(t)^3}\right|\chi(r,\theta,t)\right\rangle}{\langle\chi(r,\theta,t)|\chi(r,\theta,t)\rangle} \quad (8)$$

where $R(t)$ and $P(t)$ are the values of the classical coordinate and conjugate momentum at time t.

The accuracy of the mixed quantum/classical method depends on several factors. The first is the validity of the assumption that the dynamics of one of the H atoms is weakly coupled to the dynamics of the remaining OH molecule. In addition, because the forces on the classical particle result from an average of the Hamiltonian over $\chi(r,\theta,t)$, the quantum/classical treatment will be most accurate when this quantum wave packet is localized in coordinate and momentum space. If the wave packet bifurcates or spreads, the forces that are felt by the classical subsystem will reflect a weighted average of the forces in all regions of configuration space where the wave packet has nonzero amplitude.[3]

The previous described conditions will be met in the asymptotic region of the potential where the OH bond that is broken is represented by R and the OH bond that is propagated quantum-mechanically is the one that is not broken. Because there is equal probability for either of the two OH bonds in water to be broken, only half of the quantum wave packet will dissociate along R. The remainder of the wave packet remains localized at small values of R and moves out to larger values of r with time; this is illustrated in Figure 1. Although the two pieces of the wave packet remain reasonably localized in coordinate space, the fact that the potential has two equivalent dissociation channels leads the quantum/classical treatment to provide a poor description of the photodissociation dynamics of water.

To correct the previously mentioned deficiencies in the quantum/classical approach, we project the quantum wave packet onto two or more contributions and classical trajectories are propagated independently for each of these contributions. Following the multiple-configuration quantum approach, which was proposed by Hammerich et al.,[9] we define a set of orthogonal projection operators:

$$\mathscr{P}_n = \sum_i |\phi_{n_i}\rangle\langle\phi_{n_i}| \tag{9}$$

where $|\phi_{n_i}\rangle$ represents a vibrational eigenfunction of an isolated OH molecule. In the present case, these are constructed from linear combinations of the projection operators that are generated from the vibrational eigenfunctions of OH. We define the projection operators so that

$$\sum_n \mathscr{P}_n = 1 \tag{10}$$

and

$$\chi_n(r,\theta,t) = \mathscr{P}_n \chi(r,\theta,t) \tag{11}$$

where $\chi_n(r,\theta,t)$ represents the part of the wave packet that is localized in the nth channel. As such, the equations of motion for the multiple-configuration treatment are[45]

$$i\hbar\frac{\partial\chi(r,\theta,t)}{\partial t} = \left\{-\left(\frac{\hbar^2}{2\mu_r}\right)\frac{\partial^2}{\partial r^2} + \left[\frac{1}{2\mu_r r^2} + \frac{1}{2\mu_R R^2(t)}\right]\hat{j}^2 + V(R(t),r,\theta)\right\}\chi(r,\theta,t)$$

$$\frac{dR(t)}{dt} = \frac{P(t)}{\mu_R}$$

$$\frac{dP(t)}{dt} = -\frac{\left\langle\chi_n(r,\theta,t)\left|\frac{\partial V(R(t),r,\theta)}{\partial R} - \frac{\hat{j}^2}{\mu_R R(t)^3}\right|\chi_n(r,\theta,t)\right\rangle}{\langle\chi_n(r,\theta,t)|\chi_n(r,\theta,t)\rangle} \tag{12}$$

E. Calculating Cross Sections. The asymptotic rotation−vibration OH product state distributions are calculated from the results of the quantum simulation, using[46,47]

$$\sigma_{vj}(\omega) \propto \omega\left(\frac{\mu_R}{2\pi\hbar k_{vj}}\right)\lim_{t\to\infty}\left|\int_0^\infty dR\int_{r_{min}}^{r_{max}} dr\int_0^\pi \sin\theta\, d\theta \times \exp(-ik_{vj}R)\phi_{vj}(r)\varphi_j(\theta)\Phi(R,r,\theta,t)\right|^2 \tag{13}$$

where $\varphi_j(\theta)$ represents one of the angular momentum eigenstates of the OH and $\phi_{vj}(r)$ represents the vth vibrational wave function for OH for a given level of rotational excitation. The translational motion of H + OH is described by a plane wave with wave vector $k_{vj} = [2\mu_R(\hbar\omega + E_0 - \epsilon_{vj})]^{1/2}/\hbar$. Here, ω is the photon frequency and E_0 is the initial energy of the water molecule on the $\tilde{X}$ state. Finally, ϵ_{vj} is the energy associated with the ϕ_{vj} state.

The partial cross sections for H_2O are obtained from the mixed quantum/classical simulation, using

$$\sigma_{vj}^{Q/C}(\omega) \propto \omega\lim_{t\to\infty}\left\{\sum_{i=1}^{ntraj}\left(\frac{\mu_R}{\bar{k}^i}\right)W(R^i(0),P^i(0))\,\delta(P^i(t) - \hbar\bar{k}^i)\left|c_{vj}^i(t)\right|^2\right\} \tag{14}$$

where $c_{vj}^i(t) = \int_{r_{min}}^{r_{max}} dr \int_0^\pi \sin\theta\, d\theta\, \phi_{v,j}(r)\varphi_j(\theta)\chi^i(r,\theta,t)$. We use $\bar{\epsilon}^i = \sum_{vj} c_{vj}^i \epsilon_{vj}$ to represent the average energy of the quantum wave packet. As such, for a given photon energy $\hbar\omega$, the wave vector that corresponds to the energy available to the classical momentum, $P^i(t)$, is given by $\bar{k}^i = [2\mu_R(\hbar\omega + E_0 - \bar{\epsilon}^i)]^{1/2}/\hbar$. A more detailed description of the origins of the previously discussed expression is given in the Appendix. Finally, following Henriksen, Engel, and Schinke,[19] we replace the δ-function in eq 14 with

$$\delta(z) = \left(\frac{1}{\sqrt{\gamma^2\pi}}\right)\exp\left[-\left(\frac{z}{\gamma}\right)^2\right] \tag{15}$$

where $\gamma = 0.1$ eV.

F. Numerical Issues. The photodissociation dynamics of H_2O is studied using both the time-dependent quantum mechanics and the multiple-configuration quantum/classical methods. The potential energy surface of Partridge and Schwenke[32] is used to obtain the wave functions for water on the $\tilde{X}$ state, whereas the potential surface of Engel et al.[16] is used for the studies of the photodissociation dynamics on the $\tilde{A}$ state. Here, the initial wave packet $\Phi(R,r,\theta,t = 0)$ is obtained by multiplying the appropriate wave function for the $\tilde{X}$ state by a constant dipole moment.

In the time-dependent wave packet propagations, we use grids in R and r in the range of $0.5a_0$ to $15.5a_0$ with 128 grid points in each dimension. Thirty DVR points are used in θ. The system can dissociate along either R or r; thus, absorbing potentials are introduced in each coordinate. The absorbing potentials have the form[48]

$$\begin{aligned} f(x) &= 0 && (x_I < x)\\ &= 10y^3 - 15y^4 + 6y^5 && (x_I \le x \le x_I + \Delta x)\\ &= 1 && (x_I + \Delta x < x) \end{aligned} \tag{16}$$

where

$$y = \frac{x - x_I}{\Delta x} \tag{17}$$

The parameter x_I provides the value of r or R where the absorbing potential becomes nonzero and Δx provides the range of the absorbing potential. Here, $R_I = r_I = 11a_0$, and $\Delta R = \Delta r = 3a_0$. A time step of 100 au is used. We propagate the wave packet for 2000−3000 au, which is the time that is required for most of the wave packet to reach the asymptotic region of the potential. When part of the wave packet reaches the asymptotic region of the potential, it is projected onto the asymptotic states that are used to evaluate the cross section in eq 13 and further propagations of this part of the wave packet are performed analytically.[48,49] By varying the grid size and other propagation parameters, we are able to determine that the reported quantum-mechanical results are converged.

For the mixed quantum/classical studies, we use a 128-point grid in r in the range of $0.5a_0$ to $15.5a_0$ and 30 DVR points in θ. The same absorbing potential is used for r as was used in the three-dimensional studies. The time step for the quantum/classical simulations is limited by the time over which the equations of motion in the quantum and classical degrees of freedom in eq 12 are effectively decoupled. As such, we use a 0.2 au time step for solving the classical equations of motion and a 0.2 au time step for the quantum propagation when $R < 4a_0$. For larger values of R, a 1.0 au time step is used for the

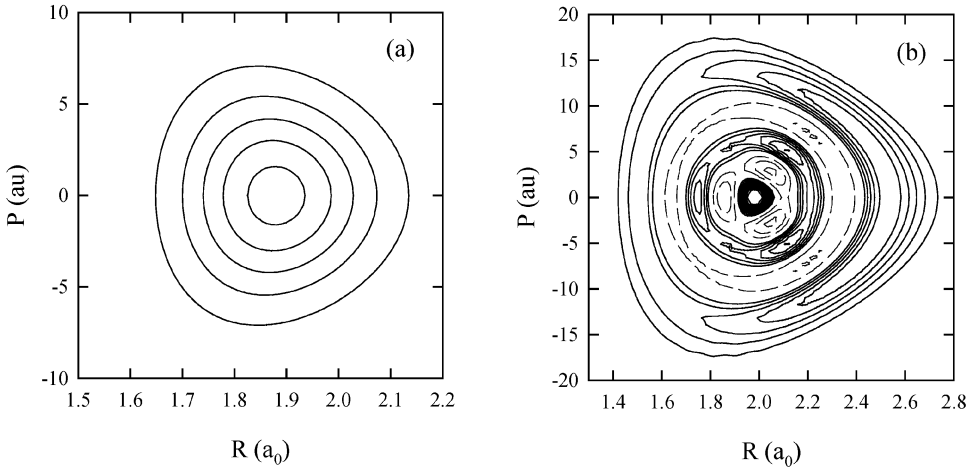

Figure 2. Contour plots of Wigner distribution function for different states with (a) zero and (b) four quanta in the OH stretch. In these plots, solid lines are used to represent positive contours and dashed lines provide the negative contours.

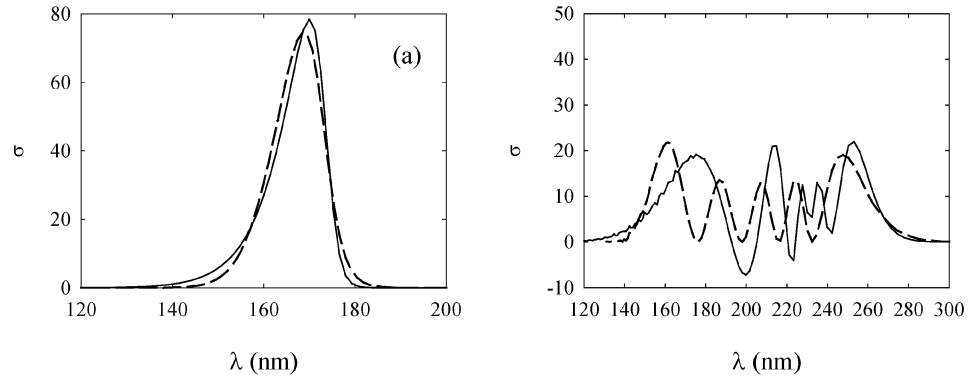

Figure 3. Comparison of the one-dimensional quantum (dashed line) and classical (solid line) cross sections for the photodissociation one of the OH bonds in water when there are (a) zero and (b) four quanta of excitation in the OH stretch.

quantum propagation and five 0.2 au time steps are taken in the classical degrees of freedom for each time we advance the quantum wave packet by 1.0 au. For both regions of the potential, we use a split operator[50] to propagate the quantum dynamics. The classical time step is required to be very small for these propagations; therefore, we have used a simple, second-order differencing scheme to solve the classical equations of motion.

The cross sections that are reported for the mixed quantum/classical simulations are based on 2000 trajectories. Here, the initial conditions for the quantum degrees of freedom are given by $\chi(r,\theta)$, whereas the initial conditions in the classical degrees of freedom are given by the Wigner distribution function in eq 7.

The quantum/classical partial cross sections are calculated when $R = 11a_0$, a distance at which the interaction potential is <1.0 cm^{-1}. Finally, it should be emphasized that the time-dependent quantum propagation and the mixed quantum/classical results are based on the same initial wave function, $\Psi_n(R,r,\theta)$.

As we mentioned previously, the Wigner distribution function for excited states is not positive for the all values of the coordinates and momenta. This is illustrated in Figure 2 for the ground state of water and the state with four quanta of excitation in the OH stretch. Despite this observation, when the distribution is integrated over R or P, the standard probability distributions in momentum and coordinate space are recovered.[51] This feature of the Wigner distribution can cause difficulties. To assess the extent of these difficulties, we compare the one-dimensional cross sections that are obtained from classical simulations using the Wigner distribution functions in Figure 2 to those obtained from quantum simulations using the same wave function. These are plotted in Figure 3. For the ground state, the agreement is very good. For the $v = 4$ state, the agreement is good for wavelengths >200 nm but deteriorates at shorter wavelengths. The implications of these deviations on an analysis of partial cross sections will be investigated in the following section.

III. Results and Discussion

A. Vibrational Ground State. To start, we will consider the photodissociation cross section for water from its ground vibrational state in two dimensions, e.g., fixed θ. As such, these simulations correspond to the wave packets that are plotted in Figure 1. The resulting cross sections are plotted in Figure 4 for the quantum approximation, as well as three quantum/classical approximations. In all these plots, the total cross section is plotted with a solid line, whereas the other lines represent partial cross sections to specific vibrational states of OH.

When only one configuration is used, we obtain the results plotted in Figure 4b. For wavelengths below ~180 nm, the quantum and single-configuration quantum/classical cross sections are in good agreement, but the quantum/classical cross sections extend to almost 220 nm, whereas the quantum results die off at ~190 nm. The cross sections that are obtained from the one-dimensional simulations (plotted in Figure 3) do not contain this feature; therefore, the errors are due to the combination of the quantum and classical treatments. In fact, the source of this problem is easily seen in the wave packet,

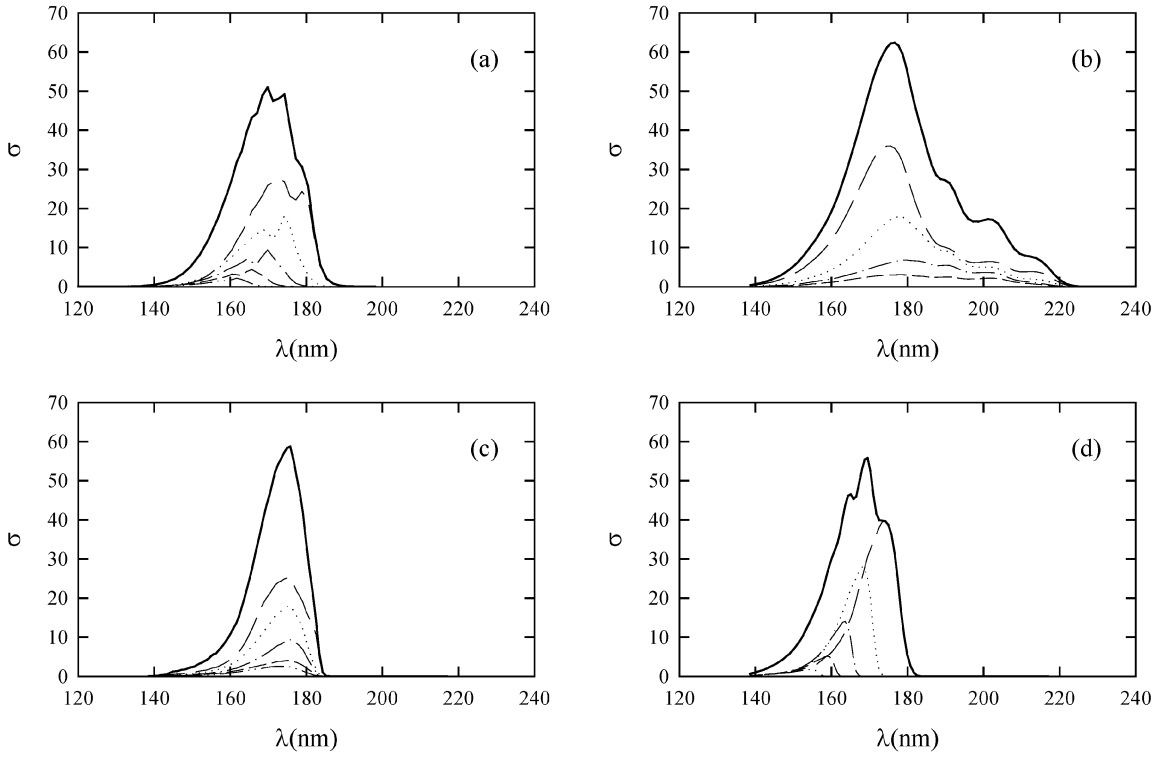

Figure 4. Comparison of the cross sections for the two-dimensional photodissociation of water (fixed θ) from the ground vibrational state obtained from the (a) quantum and (b) one-, (c) two-, and (d) six-configuration quantum/classical treatments. In all cases, the total cross section is plotted with a solid line, whereas the partial cross sections for $v = 0$, 1, 2, 3, and 4 are plotted with long dashed, dotted, dash−dotted, short dashed, and dot-dot−dashed lines, respectively.

plotted in Figure 1b. When water is initially in its ground vibrational state, there is equal probability for either of the OH bonds to break. As such, although we have set up the simulation with the assumption that the molecule will break along R, and that the OH bond that is represented by r will remain intact, there is equal probability in the simulations for either of the OH bonds to break. The trajectories that correspond to the incorrect OH bond being broken will not be described well by the quantum/classical approximation that we are using. Furthermore, some of the trajectories remain trapped in the transition state of the potential, because the effective potential that is obtained by averaging the full potential over $\psi(r,t)$ can be bound. This second feature reflects the well-known overcorrelation of the quantum and classical dynamics when such a separation is employed.[6,15]

Clearly, we need a way to separate the two parts of the wave packet shown in Figure 1b in our quantum/classical simulations. As such, in the multiple-configuration approach, one of the configurations will correspond to this dissociation channel. States with $v_{OH} > 4$ contribute little to the total cross section; therefore, we will define the nth projection operator for a n-configuration treatment, to be given by

$$\mathscr{P}_n = \sum_{i=5}^{\infty} |\phi_i\rangle\langle\phi_i| \tag{18}$$

On the basis of this observation, there are two obvious choices for the multiple-configuration treatment: a two-configuration treatment, in which

$$\mathscr{P}_1 = \sum_{i=0}^{4} |\phi_i\rangle\langle\phi_i| \tag{19}$$

and a six-configuration treatment, in which the first five configurations correspond to projection onto single OH vibrational states with $v_{OH} = 0-4$. The cross sections that result from these two approaches are ploted in panels c and d of Figure 4.

If we compare panels a and c of Figure 4, we find that the partial cross sections that are obtained from the quantum simulation are structured, whereas this structure is washed out in the two-configuration quantum/classical simulation. In addition, the partial cross sections that are obtained from the quantum simulation are shifted to shorter wavelengths as the OH vibrational energy is increased, whereas the curves have maxima at the same wavelength in the quantum/classical treatment. This second feature reflects the fact that the energy that is available to the classical degrees of freedom is determined by the conservation of energy and the average energy in the corresponding quantum degree of freedom.[6] This feature is also manifested in the single-configuration results, plotted in Figure 4b. We can eliminate this problem by running separate classical trajectories for each vibrational state of OH, as is done in the six-configuration treatment. As shown in the plot in Figure 4d, when a six-configuration treatment is used to treat the photodissociation dynamics of water, the shifts in the center of the partial cross sections are now too large and these distributions are narrower than the corresponding quantum distributions.

In summary, comparing the two types of multiple-configuration quantum/classical treatments, shown in panels c and d of Figure 4, they are both in good agreement with the quantum results. Although each of the multiple-configuration treatments has features that demonstrate deficiencies in the approximation that is used, the results are of comparable accuracy. As such, because a two-configuration treatment requires one-third of the computational resources of a six-configuration study, we will focus the remainder of the discussion on this multiple-configuration treatment.

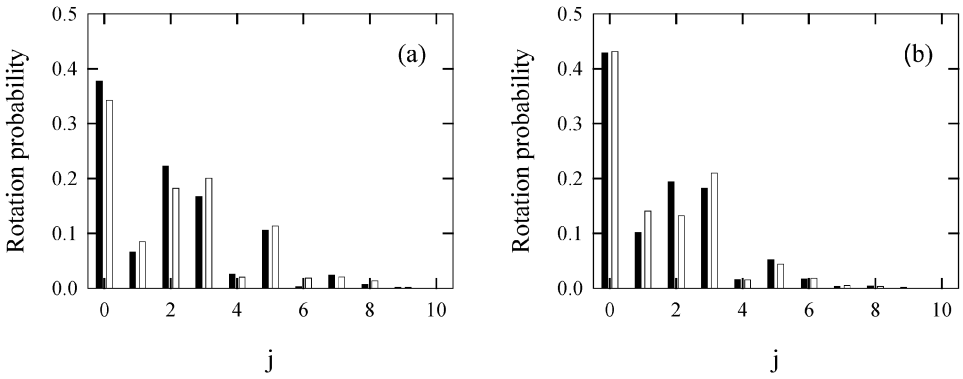

Figure 5. Partial cross sections obtained from quantum (white bars) and multiple-configuration quantum/classical (black bars) simulations of the photodissociation of water in its ground state for $\lambda =$ (a) 160 and (b) 187 nm.

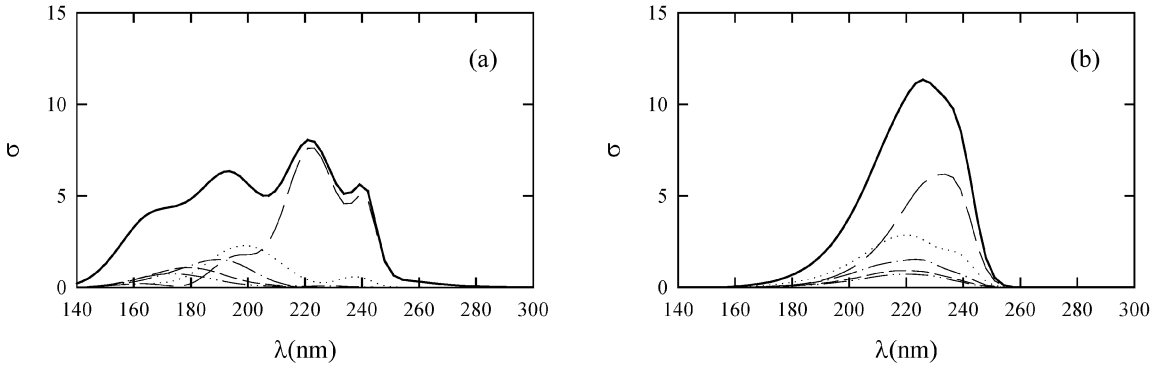

Figure 6. Comparison of the photodissociation cross sections for water when it is initially in the $|04\rangle|0\rangle$, evaluated using the (a) quantum and (b) multiple-configuration quantum/classical approaches.

We have repeated the previously described comparison for calculations of the photodissociation cross section of water in three dimensions, including the bend. The overall picture is not changed, although the structure in the quantum cross sections is eliminated almost entirely. This leads to an improvement in the agreement between the quantum and two-configuration quantum/classical results.

A more stringent test of the quantum/classical approaches can be made by breaking down the partial cross sections plotted in Figure 4 into rotationally resolved partial cross sections. These are plotted for the quantum and two-configuration simulations in Figure 5. The two wavelengths that are shown in this plot represent the red and blue tails of the partial cross section for $v_{OH} = 0$. In all cases, we have normalized the distributions so that the total probability is one. As can be seen by comparing the white lines, there are quantitative differences between the rotational distributions at these two wavelengths. The two-configuration quantum/classical simulation picks these trends quite well, even though the projection operators that were used for the quantum/classical simulations do not depend on the rotational state of OH.

B. Excited Vibrational State. As the results plotted in Figures 2 and 3 demonstrate, evaluation of the photodissociation cross sections for vibrationally excited states of water presents several additional challenges. On the other hand, the photodissociation dynamics of vibrationally excited water in isolation, or in the presence of other atoms or molecules, is a problem of experimental interest.[24,28,30,31] Because we treat the OH bond that dissociates at a different level of theory than that of the OH bond that remains intact, we use an unsymmetrized local mode wave function to approximate the initial state of the system.[52]

In a local-mode picture, the vibrational states for water are described by $|ab\rangle^s|c\rangle$. Here, a and b specify the number of quanta of excitation in each of the two OH bonds, where $a > b$ by convention, and c specifies the bending state. The superscript, $s = +$ or $-$, indicates the symmetric and antisymmetric linear combinations of the degenerate, zero-order $|ab\rangle|c\rangle$ and $|ba\rangle|c\rangle$ vibrational states. The fact that the $|40\rangle^+|0\rangle$ and $|40\rangle^-|0\rangle$ states are split by only 3.5 cm^{-1} on the Partridge and Schwenke potential[32] means that, at this level of vibrational excitation, the states that are formed by taking the sum and difference of these eigenstates are only weakly coupled by the Hamiltonian in eq 1. Therefore, these unsymmetrized $|40\rangle|0\rangle$ and $|04\rangle|0\rangle$ local-mode states should be very nearly eigenstates of eq 1. The quantum simulations discussed below are based on these unsymmetrized states. To obtain the initial conditions for the quantum/classical simulations, we perform a natural modal analysis for each of these states, as described in section II(B).

In Figure 6, we plot the quantum and quantum/classical cross sections for the dissociation of water from the $|40\rangle|0\rangle$ state. In the quantum/classical simulation, we selectively break the OH bond with zero quanta of excitation. When we analyze the quantum cross sections, we only evaluate the cross section from the channel in which the water molecule dissociates along R. Comparing the two sets of results, we find that the agreement is good for wavelengths above ~200 nm, but, for shorter wavelengths, the quantum results show significant probability for forming vibrationally excited OH. These differences between the quantum and quantum/classical cross sections reflect the overcorrelation of the partial cross sections for the different vibrational states in the two-configuration quantum/classical treatment. Despite this condition, when we analyze the rotational probabilities for three different wavelengths in Figure 7, we find

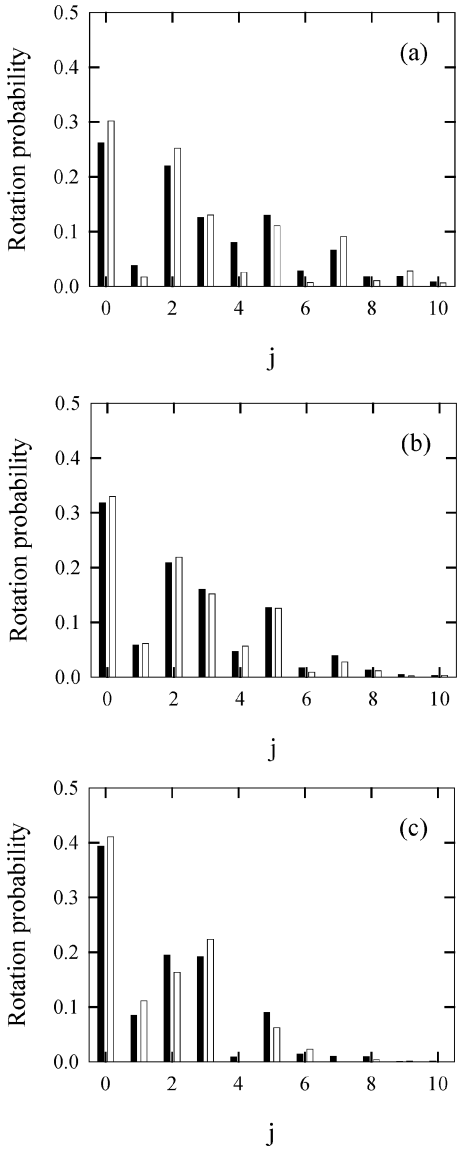

Figure 7. Partial cross sections for the photodissociation of water in the $|04\rangle|0\rangle$ state when λ = (a) 193, (b) 218, and (c) 240 nm.

that the agreement between the quantum and quantum/classical results is excellent. This is true even at 193 nm, a wavelength at which the agreement between the total cross sections is poor.

In Figures 8 and 9, we compare the quantum and quantum/classical cross sections for the photodissociation of water from the $|40\rangle|0\rangle$ state. In this case, we selectively break the OH bond with four quanta of vibrational excitation in the quantum/classical simulations, whereas in the quantum simulation, we calculate the cross sections using only the part of the wave packet that dissociates along *R*. As such, the cross sections are ~4 times as large as the cross sections shown in Figure 6. The quantum and quantum/classical simulations provide almost-identical maxima in the cross sections for this state. As in the one-dimensional classical calculations of the cross section, plotted in Figure 3b, the quantum and quantum/classical cross sections are in good agreement for wavelengths >220 nm and <180 nm; however, the agreement is less good for intermediate wavelengths. On the basis of the comparisons with the cross sections in Figure 3b, we believe that most of the differences reflect difficulties with the classical description of the cross section from vibrationally excited states, rather than a deterioration of the quantum/classical treatment for this state.

Finally, in Figure 9, we plot the rotational probability distributions for two wavelengths. One is chosen to be near the maximum in the total cross section, whereas the other is near the value of λ where the cross section is negative. In both cases, the rotational distributions calculated using the quantum/classical and quantum methods are in good agreement. Furthermore, if we add the cross sections for the two states that correspond to four quanta in one OH bond and zero in the other, the overall cross sections are in better agreement than are the separate distributions, plotted in Figures 6 and 8.

IV. Conclusions

In this paper, we have described an application of the multiple-configuration quantum/classical approach to a study of the photodissociation dynamics of water. We have shown that, although this approach does not exactly reproduce the quantum cross sections, it provides a good semiquantitative description of the dynamics. Furthermore, it provides a description of the wavelength dependence of the rotational distributions that is in excellent agreement with the quantum results. It is important to note that, because we are using a two-configuration approach, the computational demands are less than twice the demands of a single-configuration treatment.

We have also investigated the accuracy of this approach for studies of the photodissociation from vibrationally excited states of water. Again, the quantum/classical approach picks many of the most important trends in the total cross section, as well as in the rotational distribution for the ground state of OH. For example, we are able to reproduce the vibrational-state dependence on the position and the height of the maximum in the total photodissociation cross section. This is something that is not achieved by the single-configuration treatment, as is shown in the results plotted in Figure 4. We are also able to obtain semiquantitative descriptions of the rotational probability distributions and pick up the dependence of features in these distributions on the initial vibrational state of the system, as well as the wavelength at which the distribution is measured.

Clearly, there are more-accurate approaches that can be used to study three-atom systems such as water.[16,24,53−55] The purpose of the present study has been to investigate the accuracy of a multiple-configuration quantum/classical treatment of this system, to obtain insights to the level of accuracy and the types of errors we should expect when we use it to study the photodissociation dynamics for systems such as water in weakly bound complexes, for which full quantum simulations are not practical. The advantages of the quantum/classical approach for such systems can be clearly seen when we compare the computational demands for a single quantum/classical trajectory to those of a quantum wave packet simulation. Using the parameters given in section II, we find that the quantum simulation requires 3 times as much memory and 100 times as much computer processing time as a single quantum/classical trajectory. Clearly, a large number of quantum/classical trajectories will be required to obtain the same information as a single quantum wave packet simulation, and the total simulation times required to obtain the quantum/classical results shown in Figures 5−9 were twice those required to obtain the quantum results. The full advantages of the quantum/classical treatment are realized when larger systems are to be considered,because, although the memory requirements alone would make simulations of the photodissociation of water in an argon−H_2O complex prohibitive, the quantum/classical simulations of this process require 200 MB of memory, which

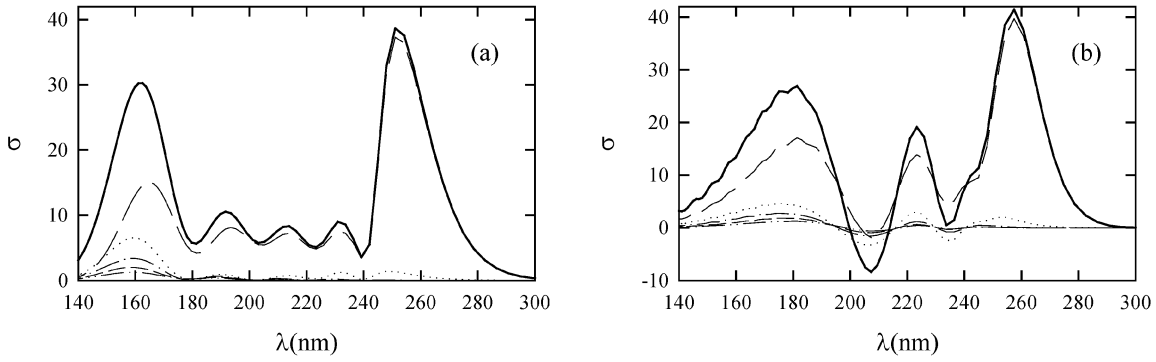

Figure 8. Comparison of the photodissociation cross sections for the $|40\rangle|0\rangle$ state of water, evaluated using the (a) quantum and (b) multiple-configuration quantum/classical approaches.

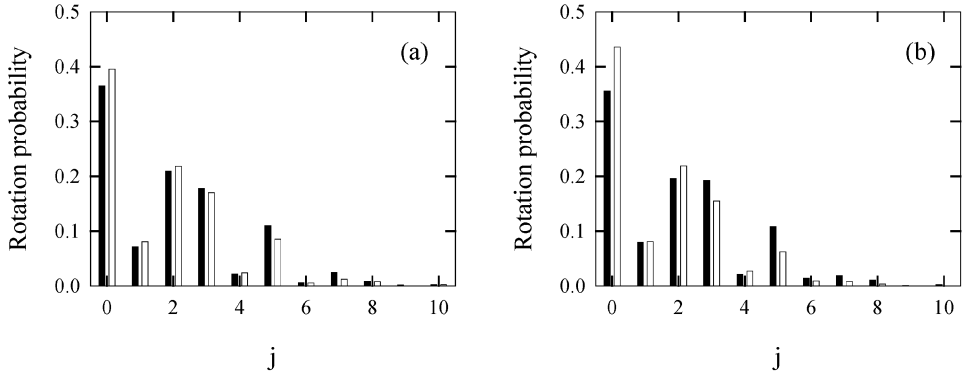

Figure 9. Partial cross sections for the photodissociation of water in the $|40\rangle|0\rangle$ state when λ = (a) 218 and (b) 266 nm.

is approximately the same amount of memory required for the quantum simulation of bare water. Furthermore, because each trajectory is propagated independently, the quantum/classical simulations are ideal candidates for being run on parallel computers.

Acknowledgment. The authors gratefully acknowledge the National Science Foundation, through Grant No. CHE-0200968, and the Dreyfus Foundation awards program for partial support of this work. We also thank Professor Lichang Wang for many helpful discussions during the course of this study.

Appendix

To evaluate the quantum/classical cross section, we begin with[43]

$$\sigma_{vj}(\omega) \propto \omega\left|\left\langle \psi_{vj}(E)\right| \exp\left(-\frac{i\hat{H}t}{\hbar}\right)\left|\Phi(0)\right\rangle\right|^2 = \omega \lim_{t\to\infty} Tr[\rho_{vj,E}\rho(t)] \tag{20}$$

where $\rho_{vj,E}$ and $\rho(t)$ are the density matrices and Tr denotes a quantum mechanical trace.

If

$$|\chi(r,\theta,t) = \sum_{vj} c_{vj}(t)|vj\rangle \tag{21}$$

then, in the quantum/classical approximation

$$\rho(t) = \sum_{i=1}^{ntraj}\Big[W\big(R^i(0), P^i(0)\big)\,\delta(R - R^i(t)) \times \delta(P - P^i(t)) \sum_{mlm'l'} c^i_{ml}(t)c^{i*}_{m'l'}(t)|ml\rangle\langle m'l'|\Big] \tag{22}$$

and

$$\rho_{vj,E} = \left(\frac{\mu_R}{2\pi\hbar\bar{k}^i}\right)\delta(P - \hbar\bar{k}^i)|vj\rangle\langle vj| \tag{23}$$

Here, v and m are used to represent the vibrational state of OH, whereas j and l provide the angular momentum quantum number.

Substituting the previously given expressions into eq 20, we find that

$$\begin{aligned}
\sigma^{Q/C}_{vj}(\omega) &\propto \omega \lim_{t\to\infty}\{Tr[\rho_{vj,E}\rho(t)]\} \\
&= \omega \lim_{t\to\infty}\left\{\sum_{v'j'}\langle v'j'|\rho_{vj,E}\rho(t)|v'j'\rangle\right\} \\
&= \omega \lim_{t\to\infty}\left\{\sum_{i=1}^{ntraj}\left(\frac{\mu_R}{\bar{k}^i}\right)\sum_{v'j'}\sum_{ml}\sum_{m'l'} W(R^i(0), P^i(0))c^i_{ml}(t) \times c^{i*}_{m'l'}(t)\langle v'j'|vj\rangle\langle vj|ml\rangle\langle m'l'|v'j'\rangle \times \int \mathrm{d}P\,\mathrm{d}R\,\delta(R - R^i(t))\delta(P - P^i(t))\delta(P(t) - \hbar\bar{k}^i)\right\} \\
&= \omega \lim_{t\to\infty}\left\{\sum_{i=1}^{ntraj}\left(\frac{\mu_R}{\bar{k}^i}\right) W(R^i(0), P^i(0))\,\delta(P^i(t) - \hbar\bar{k}^i)\left|c^i_{vj}(t)\right|^2\right\}
\end{aligned} \tag{24}$$

where $c^i_{vj}(t) = \int_{r_{min}}^{r_{max}} \mathrm{d}r \int_0^\pi \sin\theta\ \mathrm{d}\theta\ \phi_{v_j}(r)\varphi_j(\theta)\chi^i(r,\theta,t)$, $\bar{k}^i = [2\mu_R(\hbar\omega + E_0 - \bar{\epsilon}^i)]^{1/2}/\hbar$, $\bar{\epsilon}^i = \sum_{vj} c^i_{vj}\epsilon_{vj}$, $\sum_{vj}|c^i_{vj}(t)|^2 = 1$, and $P^i(t)$ is the final momentum of the ith trajectory.

References and Notes

(1) Kosloff, D.; Kosloff, R. *J. Comput. Phys.* **1983**, *52*, 35.
(2) Kosloff, R. *J. Phys. Chem.* **1988**, *92*, 2087.
(3) Alimi, R.; Gerber, R. B.; Hammerich, A. D.; Kosloff, R.; Ratner, M. A. *J. Chem. Phys.* **1990**, *93*, 6484.
(4) Gerber, R. B.; Alimi, R. *Isr. J. Chem.* **1991**, *31*, 383.
(5) Jungwirth, P.; Gerber, R. B. *Chem. Rev.* **1999**, *99*, 1583.
(6) Gerber, R. B.; Buch, V.; Ratner, M. A. *J. Chem. Phys.* **1982**, *77*, 3022.
(7) Jungwirth, P.; Gerber, R. B. *J. Chem. Phys.* **1995**, *102*, 6046.
(8) Wang, L.; McCoy, A. B. *Phys. Chem. Chem. Phys.* **1999**, *1*, 1227.
(9) Hammerich, A. D.; Kosloff, R.; Ratner, M. A. *Chem. Phys. Lett.* **1990**, *171*, 97.
(10) Matzkies, F.; Manthe, U. *J. Chem. Phys.* **1997**, *106*, 2646.
(11) Manthe, U.; Meyer, H. D.; Cederbaum, L. S. *J. Chem. Phys.* **1992**, *97*, 9062.
(12) Fang, J.-Y.; Guo, H. *J. Chem. Phys.* **1995**, *102*, 1944.
(13) Wang, L.; Clary, D. C. *Chem. Phys. Lett.* **1996**, *262*, 284.
(14) Wang, L. *J. Chem. Phys.* **1998**, *108*, 7538.
(15) Wang, L.; Meurer, W. J.; McCoy, A. B. *J. Chem. Phys.* **2000**, *113*, 10605.
(16) Engel, V.; Schinke, R.; Staemmler, V. *J. Chem. Phys.* **1988**, *88*, 129.
(17) Engel, V.; Schinke, R. *J. Chem. Phys.* **1988**, *88*, 6831.
(18) Henriksen, N. E.; Zhang, J.; Imre, D. G. *J. Chem. Phys.* **1988**, *89*, 5607.
(19) Henriksen, N. E.; Engel, V.; Schinke, R. *J. Chem. Phys.* **1987**, *86*, 6862.
(20) Guo, H.; Murrell, J. N. *Mol. Phys.* **1988**, *65*, 821.
(21) Guertler, P.; Saile, V.; Koch, E. E. *Chem. Phys. Lett.* **1977**, *51*, 386.
(22) Andresen, P.; Rothe, E. W. *Chem. Phys. Lett.* **1982**, *86*, 270.
(23) Andresen, P.; Rothe, E. W. *J. Chem. Phys.* **1983**, *78*, 989.
(24) Vander Wal, R. L.; Scott, J. L.; Crim, F. F. *J. Chem. Phys.* **1991**, *94*, 1859.
(25) Vander Wal, R. L.; Scott, J. L.; Crim, F. F.; Weide, K.; Schinke, R. *J. Chem. Phys.* **1991**, *94*, 3548.
(26) Votava, O.; Plusquellic, D. F.; Nesbitt, D. J. *J. Chem. Phys.* **1999**, *110*, 8564.
(27) Staemmler, V.; Palma, A. *Chem. Phys.* **1985**, *93*, 63.
(28) Votava, O.; Plusquellic, D. F.; Myers, T. L.; Nesbitt, D. J. *J. Chem. Phys.* **2000**, *112*, 7449.
(29) Plusquellic, D. F.; Votava, O.; Nesbitt, D. J. *J. Chem. Phys.* **1994**, *101*, 6356.
(30) Buck, U.; Ettischer, I.; Melzer, M.; Buch, V.; Sadlej, J. *Phys. Rev. Lett.* **1998**, *80*, 2578.
(31) Weide, K.; Hennig, S.; Schinke, R. *J. Chem. Phys.* **1989**, *91*, 7630.
(32) Partridge, H.; Schwenke, D. W. *J. Chem. Phys.* **1997**, *106*, 4618.
(33) Kosloff, R.; Tal-Ezer, H. *Chem. Phys. Lett.* **1986**, *127*, 223.
(34) Lill, J. V.; Parker, G. A.; Light, J. C. *Chem. Phys. Lett.* **1982**, *89*, 483.
(35) Light, J. C.; Hamilton, I. P.; Lill, J. V. *J. Chem. Phys.* **1985**, *82*, 1400.
(36) Colbert, D. T.; Miller, W. H. *J. Chem. Phys.* **1992**, *96*, 1982.
(37) Lawton, R. T.; Child, M. S. *Mol. Phys.* **1979**, *37*, 1799.
(38) McCoy, A. B.; Silbert, E. L., III. *J. Chem. Phys.* **1990**, *92*, 1893.
(39) Carter, S.; Handy, N. C. *Mol. Phys.* **1986**, *57*, 175.
(40) Colbert, D. T.; Sibert, E. L., III. *J. Chem. Phys.* **1989**, *91*, 350.
(41) Tal-Ezer, H.; Kosloff, R. *J. Chem. Phys.* **1984**, *81*, 3967.
(42) Light, J. C.; Hamilton, I. P.; Lill, J. V. *J. Chem. Phys.* **1985**, *82*, 1400.
(43) Brown, R. C.; Heller, E. J. *J. Chem. Phys.* **1981**, *75*, 186.
(44) Wigner, E. *Phys. Rev.* **1932**, *40*, 749.
(45) McCoy, A. B.; Wang, L.; Chen, F. *Faraday Discuss.* **2001**, *118*, 281.
(46) Kulander, K. C.; Heller, E. J. *J. Chem. Phys.* **1978**, *69*, 2439.
(47) Gray, S. K.; Wozny, C. E. *J. Chem. Phys.* **1989**, *91*, 7671.
(48) Neuhauser, D.; Baer, M.; Judson, R. S.; Kouri, D. J. *Comput. Phys. Commun.* **1991**, *63*, 460.
(49) Heather, R.; Metiu, H. *J. Chem. Phys.* **1987**, *86*, 5009.
(50) Feit, M. D.; Fleck, J. A., Jr. *J. Chem. Phys.* **1983**, *78*, 301.
(51) Hillery, M.; O'Connell, R. F.; Scully, M. O.; Wigner, E. P. *Phys. Rep.* **1984**, *106*, 121.
(52) Child, M. S.; Lawton, R. T. *Chem. Phys. Lett.* **1982**, *87*, 217.
(53) Engel, V.; Schinke, R.; Staemmler, V. *Chem. Phys. Lett.* **1986**, *130*, 413.
(54) Engel, V.; Staemmler, V.; Vander Wal, R. L.; Crim, F. F.; Sension, R. J.; Hudson, B.; Andresen, P.; Hennig, S.; Weide, K.; Schinke, R. *J. Phys. Chem.* **1992**, *96*, 3201.
(55) Wang, D.; Zhu, W.; Zhang, J. Z. H.; Kouri, D. J. *J. Chem. Phys.* **1997**, *107*, 751.